ICAS-88-5.9.3

MODELING OF VORTEX DOMINATED FLOWFIELDS IN THE EULER FORMULATION

K. D. Lee and S. A. Brandt
University of Illinois
Urbana, Illinois

Abstract

This paper describes a computational approach which uses the Euler formulation for vortex dominated flowfields around highly swept wings coupled with an algebraic model derived from the Navier-Stokes equations to represent the viscous physics within the vortex core. The approach also accounts for viscosity effects near the wing surface through a modified surface boundary condition. With the developed viscous model, the Euler formulation can give better prediction of leading edge separation, vortex bursting, and secondary vortex formation. Results for several cases are compared with those from wind tunnel tests and Euler and Navier-Stokes computer codes.

I. Introduction

Vortex aerodynamics has played an important role in the development of high performance aircraft in recent years. Computational fluid dynamics has been an attractive alternative to wind tunnel testing for vortical flow research. Many computational efforts have been made to predict the steady vortex dominated flowfield based on the Euler and Navier-Stokes equations.[1-7] Available simulation technologies and physical aspects were reviewed by several authors.[8,9] Some investigators were able to simulate vortex breakdown and generate secondary vortices.[10,11] Effects of grid topology and grid density on the resulting flow solutions were also studied.[1,11,12] While significant progress has been made, present technologies still have many limitations for practical applications.

Flow phenomena associated with leading-edge separation on a delta wing are extremely nonlinear and viscous, and the Navier-Stokes equations must be used to represent the complex physics. Navier-Stokes codes, however, require grid systems which have cell dimensions compatible with the characteristic length scale for viscous effects. This requirement for fine grids, especially for high Reynolds number flows, leads to large memory and computer time requirement, making the solutions relatively expensive. The resulting solutions are contaminated by the presence of numerical viscosity which is a function of the grids used and in some cases can be greater than the physical viscosity. The Navier-Stokes formulation is also hampered by the lack of an adequate turbulence model.

Codes which solve the Euler equations are generally less expensive because they do not attempt to model viscosity effects. This cost advantage is partly due to the use of simpler equations but primarily due to the use of coarser grids than those used by Navier-Stokes solvers. Although the Euler formulation can give adequate representation of most portions of the flowfield, it often fails to resolve the details of vortex core dynamics. If defined in the same direction as the physical viscosity, the numerical viscosity in Euler codes can trigger such viscous effects as leading edge separation and vortex bursting but can not represent the physics quantitatively. Although Euler solutions can produce a flow structure similar to that of the actual viscous physics, many important flow features cannot be captured at the correct flow conditions with Euler codes.

This paper describes a method which uses the Euler formulation but includes the viscous physics through a vortex core model and a modified surface boundary condition. The approach can thus provide an improved simulation capability for the analysis of vortical flows including vortex breakdown and secondary vortices at comparatively low costs. The modified surface boundary condition also improves the ability of Euler codes for predicting the angle of attack at which a leading edge vortex starts to appear on wings with round leading edges. Two computer codes, FLO57 and ARC3D, were modified for this study.[13,14] Capabilities and limitations of the codes for vortical flow applications are first evaluated in the next section. Simple viscous models are then developed based on analytic simplification of the Navier-Stokes equations. Those models are next incorporated into the Euler codes and evaluated for several test cases. Results are compared with those from experiments and from conventional Euler and Navier-Stokes solutions.

II. Assessment of Current Euler Technology

A computational experiment was performed to evaluate the Euler codes chosen for the intended vortical flow study. The flowfield considered was a simple three-dimensional domain with a vortex filament introduced in the direction of the free stream near an infinitely large flat wing and a plane of symmetry. This test case excluded the complications of real delta wings such as the vortex creation mechanism and pressure gradients. The parameters monitored were vortex strength, vortex location, vortex core size, and axial velocity component inside the core. Computational field grids were constructed inside a rectangular box in a quarter space. A solid wall boundary condition was imposed at the bottom face of the box and a mirror image condition on the vertical plane of symmetry. The upstream boundary condition of the box was given by a swirling vortex flow added to a uniform free stream. The other three box faces were specified with farfield boundary conditions. The flowfield was initialized with a flow identical to that at the upstream boundary. Both codes gave essentially the same results, revealing several concerns in modeling vortex flows.

Numerical Vortex Core

All Euler codes include numerical viscosity built-in through finite discretization and added externally for computational stability. Euler codes cannot accommodate a purely inviscid vortex which contains a singularity at the center, unless it is fitted. The vortex must have a rotational core as in the Rankine vortex and the size of the core depends on numerical viscosity, not on physical viscosity, in the Euler formulation. The amount of numerical viscosity is determined by the numerical algorithm adopted, the grid used, and the variation of flow variables. Hence, there is a limitation in the vortex core size which can be resolved by an Euler code on a given grid. The core size here is measured by the number of grid cells across the core. Any core smaller than this limit will be diffused. Numerical diffusion also occurs in the Navier-Stokes formulation, especially when larger grid cells are used for high Reynolds number flows. For both Euler codes tested, the minimum acceptable core size was surprisingly large. The peak circumferential velocity component due to the vortex was found about four grid cells away from the cell containing the vortex center. When a vortex was introduced through the upstream boundary with the core size smaller than this limit, the core grew to the limit size in three to five cells downstream. In Figure 1, profiles of circumferential velocity and circulation for the limit size obtained from the computational experiment are compared with the Rankine vortex and the model used by Mager.[15] Note that the total circulation around a vortex is constant outside the core. Figure 2 shows that the core area which contains significant vorticity extends at least five cells in radius. The corresponding pressure distribution obtained is given in Figure 3.

Grid Induced Bursting

The next observation concerns the influence of non-uniform stretched grids. Several different stretched grids were fitted inside a rectangular box, with denser spacing near the solid wall and the core region. The local grid refinement along the vortex core allowed a smaller core size. Grid stretching and grid skewing had little effect on flow solutions except when the vortex tube passed through a region of the grid where the cells were expanding. Expanding grids enlarged the vortex core. Since the flow solver preserved the total circulation of the vortex, this non-physical growth of the core caused reduced circumferential velocity component and increased core pressure in proportion to the enlargement of the cells. For a grid with a size expansion ratio of 1.22 in the axial direction, the resulting adverse pressure gradient along the vortex core caused a reversal in the axial velocity component inside the core, as in vortex bursting.

Identical flow conditions were tested on two different grids. Figure 4 shows the two grids. Grid A is locally skewed but not stretched in the region of the vortex core and Grid B is stretched near the vortex core and expanding in the axial direction along the core. Figure 5 compares the axial variation of the static pressure along the vortex core for the two grid systems, exhibiting a negligible axial pressure gradient for Grid A and a significant gradient for Grid B. The velocity vectors in the vertical plane which contains the vortex core are plotted with arrows in Figure 6. The solution for Grid A does not exhibit axial flow reversal but Grid B produces a large recirculating zone.

These results demonstrate that non-physical mechanisms in Euler solvers can determine the vortex core size and can contribute to vortex bursting. A vortex core model derived from the Navier-Stokes equations can predict pressure and velocity fields based on physics instead of relying on numerics. Addition of this model to Euler solvers will provide a useful tool for analyzing vortex dominated flows.

III. Vortex Core Model

A model for the vortex core is derived from the steady, incompressible Navier-Stokes equations written for the cylindrical coordinate system centered on a vortex core. The modeling process is similar to that developed by Mager[15] and Krause,[16] but the present model includes non-axisymmetric effects due to image vortices. The vortex is assumed to be slender and close to a wing surface and a plane of symmetry. The velocity components u,v and w are defined in the x, r, and θ coordinates which correspond to axial, radial, and circumferential directions. The following non-dimensional parameters are defined:

$$\epsilon = \frac{\delta_{ref}}{L}$$

$$Re = \frac{\rho U_\infty L}{\mu}$$

where L is the reference axial length scale of the vortex and δ_{ref} is the reference vortex core radius at $x = L$. ρ and μ are density and viscosity of the air respectively and U_∞ denotes the freestream velocity. Length, velocity, and pressure are normalized by L, U_∞, and ρU_∞^2 respectively. As in the boundary layer equations, the radial coordinate and its velocity component are scaled by the small parameter ϵ.

The vortex core diameter is assumed to be of the order of the square root of the Reynolds number. After eliminating the terms which become negligible for large Reynolds numbers and the terms involving in the circumferential direction, the equations of motion become:

$$\frac{\partial(ru)}{\partial x} + \frac{\partial(rv)}{\partial r} = 0 \qquad (1a)$$

$$u\frac{\partial u}{\partial x} + v\frac{\partial u}{\partial r} = -\frac{\partial p}{\partial x} + \frac{1}{Re\epsilon^2}\left\{\frac{1}{r}\frac{\partial}{\partial r}\left(r\frac{\partial u}{\partial r}\right)\right\} \qquad (1b)$$

$$\frac{w^2}{r} = \frac{\partial p}{\partial r} \qquad (1c)$$

$$u\frac{\partial w}{\partial x} + v\frac{\partial w}{\partial r} + \frac{vw}{r} = \frac{1}{Re\epsilon^2}\left\{\frac{\partial}{\partial r}\left(\frac{1}{r}\frac{\partial}{\partial r}(rw)\right)\right\} \qquad (1d)$$

The above equations are integrated algebraically by defining axial and circumferential velocity profiles within the vortex core. Here the velocity profile implies the shape of the velocity distribution in the radial direction. As seen in Figure 1, the velocity profile defined by Mager[15] matches well with those obtained from Euler solutions and is adopted for the integration. Also included is the influence due to the image vortex filaments associated with the wing surface boundary and the plane of symmetry. For this purpose, the Cartesian coordinate system is used with X, Y, and Z as streamwise, spanwise, and vertical coordinates respectively. In this coordinate system, two non-dimensional distances and two angles are defined as follows:

$$l_Y = \frac{Y_{core} - Y_{wing}}{\delta_{ref}} \qquad l_Z = \frac{Z_{core} - Z_{symm}}{\delta_{ref}}$$

$$\phi_Y = \tan^{-1}\left(\frac{dl_Y}{dx}\right) \qquad \phi_Z = \tan^{-1}\left(\frac{dl_Z}{dx}\right).$$

First, with the specified circumferential velocity profile, equation (1c) is integrated from the core center, $r = 0$, to the edge of the core, $r = \delta$. Then the pressure at the vortex center can be given by

$$p(x,0) = p(x,\delta) - K_a\frac{\Gamma^2}{a} + K_i\Gamma^2 C_\phi. \qquad (2)$$

The vortex core area a and the circulation Γ are defined as

$$a = \pi\delta^2 \qquad \text{and} \qquad \Gamma = 2\pi\delta w_\delta$$

respectively, where the subscript δ denotes the value at the core boundary. In equation 2, C_ϕ is the influence of the image vortices given by

$$C_\phi = \frac{\cos\phi_Y}{l_Y^2} + \frac{\cos\phi_Z}{l_Z^2} - \frac{\cos\phi_Y\cos\phi_Z}{l_Y^2 + l_Z^2}. \qquad (3)$$

The coefficient K_a depends on the choice of the circumferential velocity profile and K_i accounts for the influence of image vortices.

It is assumed that the velocity profiles are similar in the axial direction, with the core diameter δ and the core edge axial velocity u_δ as the similarity parameters. Using these parameters, the radial velocity profile can be obtained by integrating equation (1a) with respect to the radial direction. With the three components of velocity profiles known, equation (1d) is then integrated over the area of the vortex core to obtain:

$$\frac{1}{a}\frac{da}{dx} = \frac{K_1}{\Gamma}\frac{d\Gamma}{dx} - \frac{K_2}{u_\delta}\frac{du_\delta}{dx} + \frac{K_3}{Re\epsilon^2 a u_\delta} \qquad (4)$$

where the values of K_1, K_2, and K_3 depend on the velocity profiles chosen. For the Rankine vortex circumferential velocity profile, K_2 and K_3 are zero and K_1 is one. In this case, equation (4) gives

$$a \propto \Gamma. \tag{5}$$

For complex velocity profiles, it is more difficult to integrate equation (4). If the last term in equation (4) is assumed to be independent of x, then it can be integrated to give:

$$a = K_\theta \frac{\Gamma^{K_1}}{u_\delta^{K_2}}(x - x_o) \tag{6}$$

where K_θ is a core growth parameter which depends primarily on the product $Re\epsilon^2$ and x_o comes from the integration constant. Equation (6) serves as a model for the growth of the physical vortex core based on velocity profiles and parameters measured from the Euler solution.

Next, the circumferential velocity profile is assumed to be close to that of the Rankine vortex in order to approximate the radial distribution of pressure with

$$p(x,r) = p(x,0) + \left(\frac{r}{\delta}\right)^2 (p(x,\delta) - p(x,0)). \tag{7}$$

Using equations (2) and (7), equation (1b) is integrated over the area of the core to get the one-dimensional relation along the vortex core to give

$$u_0 \frac{du_0}{dx} + \frac{dp_0}{dx} = -K_a\left(\frac{\Gamma}{a}\frac{d\Gamma}{dx} - \frac{\Gamma^2}{a^2}\frac{da}{dx}\right) + K_i\left(\Gamma\frac{d\Gamma}{dx}C_\phi - \frac{\Gamma^2}{2a}\frac{da}{dx}C_\phi + \frac{\Gamma^2}{2}\frac{dC_\phi}{dx}\right) \tag{8}$$

where the subscript 0 designates core center values.

It is worthwhile to point out that the contribution of the viscous term disappears in the integration if the axial velocity profile is defined with zero slopes at the center and the edge of the core. Note that the coefficients K_a and K_i are functions of the velocity profiles and the location of the vortex core. If the velocity profiles of the viscous core and those in Euler solutions are similar, then the major discrepancy of the Euler formulation is primarily due to the non-physical estimation of the core size and the core growth rate. Therefore, the non-physical vortex core in Euler solutions can be replaced with a core that is derived from viscous physics, as given in equation (8). This is in effect equivalent to an addition of the difference between the model and the Euler solution as a source term into the Euler formulation. The difference can be given as:

$$\left(u_0\frac{du_0}{dx} + \frac{dp_0}{dx}\right) - \left(u_0\frac{du_0}{dx} + \frac{dp_0}{dx}\right)_E = -K_a\left\{\frac{\Gamma}{a}\frac{d\Gamma}{dx}\left(1 - \frac{a}{a_E}\right) - \frac{\Gamma^2}{a^2}\left(\frac{da}{dx} - \frac{a^2}{a_E^2}\frac{da_E}{dx}\right)\right\} - K_i\frac{\Gamma^2}{2a}C_\phi\left(\frac{da}{dx} - \frac{a}{a_E}\frac{da_E}{dx}\right) \tag{9}$$

where the subscript E denotes flow quantities measured in the Euler solution. Similarly, the correction to pressure at the core center is given by

$$p(x,0) - p(x,0)_E = -K_a\frac{\Gamma^2}{a}\left\{1 - \left(\frac{a}{a_E}\right)^2\right\} + K_i\Gamma^2\left(1 - \frac{a}{a_E}\right)C_\phi. \tag{10}$$

Equation (9) provides a momentum source term for use in the axial momentum equation in the Euler solver. Again the control parameters K_θ, K_a, and K_i depend primarily on the velocity profiles of the physical vortex. Equation (10) provides a correction to the vortex core pressure in the Euler solution based on the ratio of the size of the model core to the size of the core in the Euler solution.

IV. Surface Boundary Condition

Leading edge vortices are created by boundary layer separation near the leading edges of highly swept wings. Without viscous models for the shear layer of the three-dimensional separation, Euler solvers create the leading edge separation by numerical diffusion, which is again a function of grid quality and grid size. Also, the strength of vorticity depends on the location of separation, which cannot be determined a priori for wings with round leading edges.

The momentum equations for the control volume next to the wing surface require the knowledge of pressure on the wing surface. Two different methods for estimating the pressure on the wing surface were tested. The first method uses the normal momentum equation from the Euler formulation to extrapolate pressure from the cell center down to the wing surface. When this method is used, the appearance of leading edge vortices in the flow solution was delayed to higher angles of attack than those obtained from wind tunnel tests. The second method equates the pressure at the wing surface with the pressure at the center of the boundary cell, by assuming zero normal pressure gradient as in the boundary layer. When this method is used, the vortices start to appear at lower angles of attack. Figure 7 compares wing surface pressure contours for a range of angles of attack measured in a wind tunnel[17] with contours from Euler solutions using the two different boundary conditions. When coarser grids are used, the difference between the computational results and the wind tunnel results becomes even larger.

The flow phenomena inside the viscous shear layer involving leading edge separation are too complex to model with simple physics. The flowfield involves many difficult features including the mechanism for creation of leading edge vortices, reattachment of the primary vortex, appearance of a secondary vortex separation, etc. Instead of attempting to model the difficulties, a simple model is used in this study to include a characteristic influence of the viscosity effects near the wing. Two major characteristics, shear layer thickness and wall shear stress, are identified and modeled with the formula borrowed from the incompressible turbulent boundary layer on a flat plate. That is, the wall shear layer thickness and the skin friction coefficient are defined from

$$\delta_{wall} = \frac{K_\delta l}{(Re_{local})^{0.2}} , \qquad (11)$$

$$C_f = \frac{K_\tau}{(Re_{local})^{0.2}} \qquad (12)$$

where Re_{local} is the local Reynolds number based on the distance l measured from the apex of a delta wing. The coefficients K_δ and K_τ are input specified constants with values of 0.37 and 0.074 respectively for the flat plate. The shear stress effect is added into the momentum equations in the direction of the surface velocity vector as source terms. The shear layer thickness effect is accounted for in the surface pressure estimation by using

$$p_{wall} = p_{cell} - \frac{dp}{dn}(\Delta - \delta_{wall}) \qquad (13)$$

where p_{cell} is the pressure at the neighboring boundary cell, dp/dn is the pressure gradient in the normal direction, and Δ is the normal distance between the two points. If δ_{wall} is set to zero, the equation implies that the wall pressure is obtained through a purely inviscid calculation.

V. Results

Model Implementation

The vortex core model was incorporated into the Euler solvers as a separate subroutine and accessed periodically. The total circulation or vortex strength and the Euler vortex core size are determined from Euler solutions at each axial location along the vortex. The vortex strength is obtained by evaluating the vorticity fluxes through the surfaces of each cell and summing them. The area of the vortex core is measured from the cross sectional areas of the cells which contain vorticity of strength above a given threshold level. The center of the vortex at each axial station is identified as the cell with a local minimum static pressure and a local maximum vorticity flux. Locating the vortex center establishes the values of C_ϕ in equation (3).

The momentum source term in the axial momentum equation and the correction to the pressure at the vortex center are obtained from equations (9) and (10). These quantities are added to the flow solver for subsequent iterations. To avoid destabilizing the solution process, the momentum source terms are not just applied to the cell at the vortex center. The source terms for the neighboring cells are scaled in accordance with their distance from the center following a profile similar to the axial velocity profiles used by Mager. In order to reduce computational costs, these corrections were updated every 30 to 50 iterations.

The viscous layer model for the surface boundary condition was also incorporated into the Euler solver. The pressure at the surface was defined using equation (13) to include the viscous layer thickness effect. The shear stress in equation (11) defines source terms for the boundary cells. The source terms are added into the Euler equations in the direction which is approximated as being parallel to the surface velocity vector. As in the vortex core model, the corrections for the surface boundary condition model were updated periodically.

Model Evaluation

The effectiveness of the vortex core model was evaluated for the test problem discussed in Section II. As seen in Figure 6, a non-physical flow reversal in the axial direction was experienced when a vortex flowed into grids with steadily increasing cell size. The developed model can eliminate or minimize the grid dependency of flow solutions. Figure 8 shows axial velocity vectors obtained from the Euler solver with the core model, on the same grids shown in Figure 4. When a zero rate of growth of the physical core was assumed, the Euler code alone produced axial flow reversal on Grid B due to grid-induced core growth. The vortex core model has eliminated the grid-induced axial velocity defect, by linking core pressure to physical core size instead of grid dependent core size.

On the other hand, the experiment with the model suggests that, if a sufficient rate of growth of the physical core is assumed, the model could produce axial flow reversal which cannot be captured with the Euler formulation. Figure 8 also illustrates a successful demonstration of this capability on a uniform grid, Grid A. Unlike the Euler solver alone, the Euler code with model can produce a flow reversal depending on parameter values which determine the viscous core.

Swept Wing Analyses

THe developed core model was implemented to assess its ability in predicting the onset of bursting on four different delta wings. A grid with H-O topology was used around flat plate delta wings with sweep angles varying from 55 to 76 degrees. Figure 9 shows a typical grid used for the test. Figure 10 shows bursting location versus angle of attack curves for the Euler solver with the vortex core model for four different wings, compared with results from wind tunnels,[18,19] Euler solvers alone, and Navier-Stokes solvers.[20] For all these tests, the parameters K_θ, K_α and K_i were held constant. For each wing tested, the Euler code with model was able to produce results which were in closer agreement with the wind tunnel tests and the Navier-Stokes codes than did the Euler solver alone. Figure 11 shows spanwise surface pressure coefficient distributions at the midpoint of the root chord of an aspect ratio 1 delta wing at 20.5 degrees angle of attack. At this angle of attack, the vortex does not burst over any part of the wing. The C_p curve predicted by the Euler solver with the core model is compared with curves from the Euler solver alone and from Navier-Stokes simulations[20] and wind tunnel tests.[21] Note that neither Euler solvers captured the secondary vortex influence on the C_p curve which is evident in the wind tunnel data and Navier-Stokes solutions. However the vortex core model does allow the modified Euler code to predict the peak of the C_p curve in closer agreement with experiment. Figure 12 compares velocity vectors in the horizontal plane containing the vortex for the same wing at 40 degrees angle of attack. The result from the Euler code alone shows the bursting point at the axial station about 70% root chord downstream of the wing apex. The Euler code with model gives the bursting point at about 30% root chord, which does agree better with Navier-Stokes results. Figure 13 compares the corresponding Cp curves for the two solutions at 50% root chord. The vortex at that station has burst in the Euler with model solution, but not in the Euler alone solution. Note the flattening of the Cp curve when bursting has occurred.

Next, the surface boundary condition with the viscous layer model was tested on the arrow wing used for the evaluation of the limitations of existing boundary conditions. Figure 14 illustrates the effect on surface pressure distribution of changing K_δ while holding the Reynolds number based on the root chord equal to the Reynolds number of the wind tunnel tests. A value of 2.1 for K_δ appears to give the best results. Figure 15 compares surface pressure plots from wind tunnel tests with those from an Euler solver with the viscous layer model surface boundary condition for a range of angles of attack.

A preliminary test was conducted using the simple shear stress model discussed in Section IV. In the model, effects of velocity defects in the viscous layer were included as momentum source terms in boundary cells. Figure 16 compares two crossflow velocity vector plots for a 65 degree swept delta wing with round leading edges. Figure 16a is for the original Euler solver, while Figure 16b is for the Euler solver with the wall stress model. Figure 16b shows the appearance of a secondary vortex in the flowfield. The location and strength of this secondary vortex are in qualitative agreement with results from Navier-Stokes solutions[20] and wind tunnels.[21] Because such secondary vortices are not normally seen in Euler solutions[3,4], these preliminary results are encouraging and further investigation of the viscous layer model concept is required.

Conclusions

A computational approach has been developed which incorporates a viscous model for vortex core

dynamics into Euler solvers. The model provides corrections to the flow quantities in Euler calculations. The corrections are added into the Euler equations as source terms. The combination of Euler code and core model has been shown to give predictions of vortex bursting points on delta wings which are in better agreement with wind tunnel tests and Navier-Stokes solutions than can be achieved by an Euler code alone. Surface pressure predictions are also improved. The model reduces the effects of grid stretching and artificial viscosity which may cause vortex bursting in Euler solutions and catches vortex bursting as in Navier-Stokes solutions. These capabilities are achieved at a very modest cost.

A simple method has also been developed to include viscous physics in the surface boundary condition used in Euler solvers. An approximation of the total pressure loss in the viscous layer near the wing surface provides a boundary condition which is closer to the actual physics. Prediction of leading edge separation and vortex rollup on highly swept wings with rounded leading edges is also improved. The use of a more refined model for the viscous layer would further enhance the performance of the method. It has also been demonstrated that inclusion of momentum defect effects near the wing surface can lead to the appearance of a secondary vortex in the Euler solution.

The technology discussed here is well suited for additional development. Further refinement of the present models and fine tuning of the control parameters are ongoing. The models can be extended to include higher order effects.

Acknowledgment

The authors wish to thank Tedd Pierce and James Loellbach for their technical assistance in preparing this paper. Advice and encouragement from Dr. Raymond Cosner and Dr. August Verhoff of McDonnell-Douglas are also gratefully acknowledged. This research was partially supported by the McDonnell-Douglas Aircraft Company.

References

1. Raj, P. and Long, L. N., "An Euler Aerodynamic Method for Leading-Edge Vortex Flow Simulation," Vortex Flow Aerodynamics, NASA CP 2416, Vol. 1, Oct. 1985, pp. 263-281.
2. Murman, E. M. and Rizzi, A., "Applications of Euler Equations to Sharp Edge Delta Wings with Leading Edge Vortices," AGARD Symposium on Application of Computational fluid Dynamics in Aeronautics, Aix-en-Provence, France, April 1986.
3. Rizzi, A., Drougge, G., and Purcell, C. J., "Euler Simulation of Shed Vortex Flows Over the 65 Degree Delta Wings," Symposium on International Vortex Flow Experiment on Euler Code Validation Proceedings, Nov. 1986, pp. 289-343.
4. Sirbaugh, J. R., "Euler Analysis of the AFWAL 65 Degree Delta Wing," Symposium on International Vortex Flow Experiment on Euler Code Validation Proceedings, Nov. 1986, pp. 245-268.
5. Newsome, R.W. and Thomas, J. L., "Computation of Leading Edge Vortex Flows," Vortex Flow Aerodynamics, NASA CP 2416, Vol. 1, Oct. 1985, pp. 305-330.
6. Rizzetta, D. P. and Shang, J. S., "Numerical Simulation of Leading-Edge Vortex Flows," AIAA Journal, Vol. 24, No. 2, Feb. 1986, pp. 237-245.
7. Kandil, O. A., Chuang, A. H., and Shifflette, J. M., "Finite-Volume Euler and Navier-Stokes Solvers for Three-Dimensional and Conical Vortex Flows Over Delta Wings," AIAA Paper 87-0041, Jan. 1987.
8. Hoeijmakers, H. W. M., "Methods for Numerical Simulation of Leading Edge Vortex Flow," Studies of Vortex Domi- nated Flows, Springer-Verlag, 1987, pp. 223-269.
9. Newsome, R. W. and Kandi, O. A., "Vortical Flow Aerodynamics - Physical Aspects and Numerical Simulation," AIAA Paper 87-0205, Jan. 1987.
10. Fujii, K. and Schiff, L.B., "Numerical Simulation of Vortical Flows Over a Strake-Delta Wing," AIAA Paper 87-1229, Jan. 1987.
11. Hsu, C. H. and Liu, C. H., "Navier-Stokes Computation of Flow Around a Round-Edged Double-Delta Wing," AIAA Paper 88-2560-CP, June 1988.
12. Hitzel, S. M., "Wing Vortex-Flows Up Into Vortex-Breakdown - A Numerical Simulation," AIAA Paper 88-2518-CP, June 1988.
13. Jameson, A., Schmidt, W., and Turkel, E., "Numerical Solutions of the Euler Equations by Finite Volume Methods Using Runge-Kutta Time-Stepping Schemes," AIAA Paper 81-1259, June 1981.
14. Pulliam, T. H., "Euler and Thin Layer Navier-Stokes Codes: ARC2D, ARC3D," Notes for Computational Fluid Dynamics User's Workshop, Tullahoma, Tennessee, March 1984.
15. Mager, A. "Dissipation and Breakdown of a Wingtip Vortex," Journal of Fluid Mechanics, Vol. 55, part 4, 1972, pp. 609-628.
16. Krause, E., "A Contribution to the Problem of Vortex Breakdown," Computers and Fluids, Vol. 13, No.3, pp. 375-381.
17. Manroe, M. E., Manning, K. J. R., Halstaff, T. H., and Rogers, J. T., "Transonic Pressure Measurements and Comparison of Theory to Experiment for an Arrow-wing Configuration," NASA CR 2610, August 1976.
18. Wentz, W. H. and Kohlman, D. L., "Vortex Breakdown on Slender Sharp-Edged Wings," Journal of Aircraft, Vol. 8, No. 3, March 1971, pp. 156-161.
19. Payne, F. M. and Nelson, R. C., "An Experimental Investigation of Vortex Breakdown on a Delta Wing," Vortex Flow Aerodynamics, NASA CP 2416, Vol. 1, Oct. 1985, pp. 135-161.
20. Hartwich, P.-M., Hsu, C. H., Luckring, J. M., and Liu, C. H., "Numerical Study of the Vortex Burst Phenomenon for Delta Wings," AIAA Paper 88-0505, Jan. 1988.
21. Hummel, D., "On the Vortex Formation Over a Slender Delta Wing at Large Angles of Incidence," AGARD-CP-247, Paper No. 15, 1978.

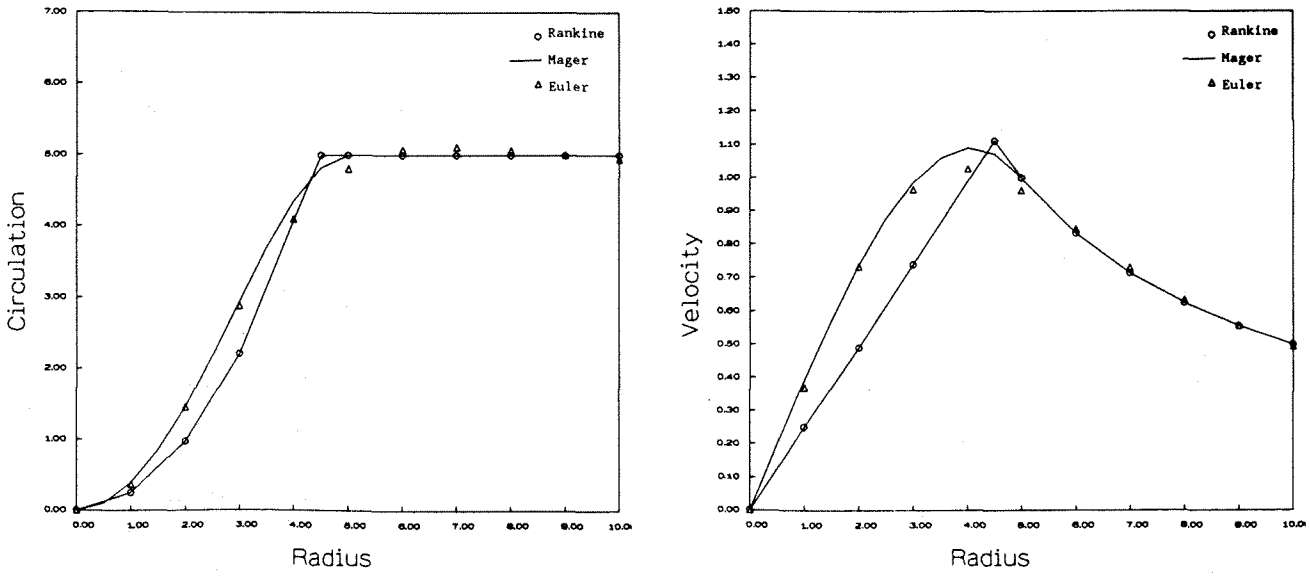

Figure 1. Circulation and circumferential velocity profiles.

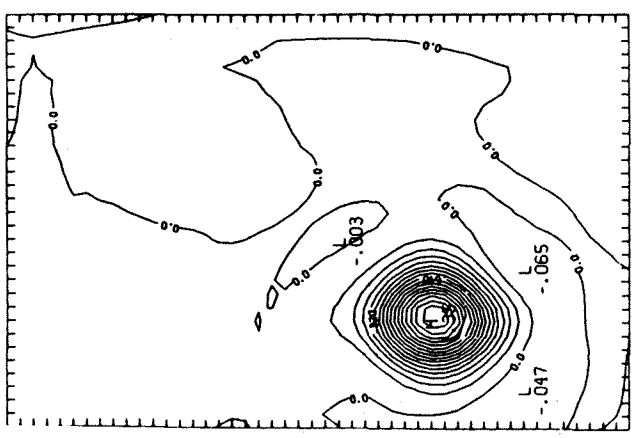

Figure 2. Crosflow plane circulation contours.

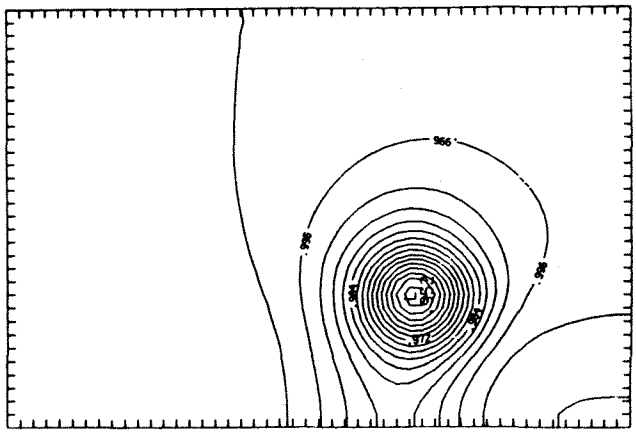

Figure 3. Crossflow plane pressure contours.

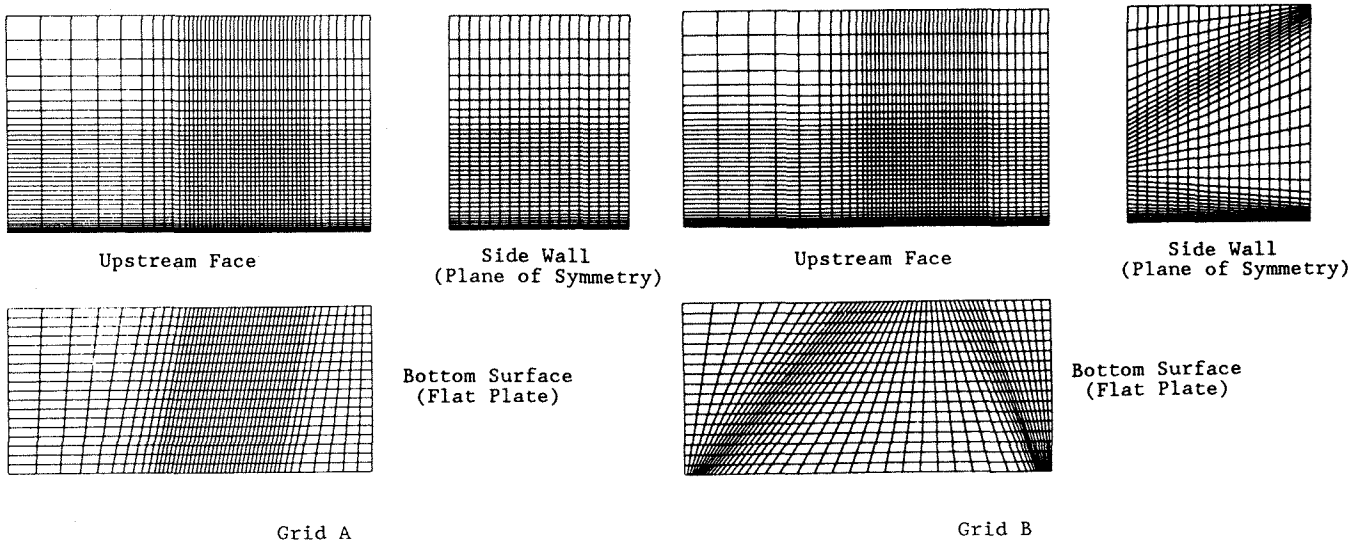

Figure 4. Three views of skewed and stretched grids in a rectangular box.

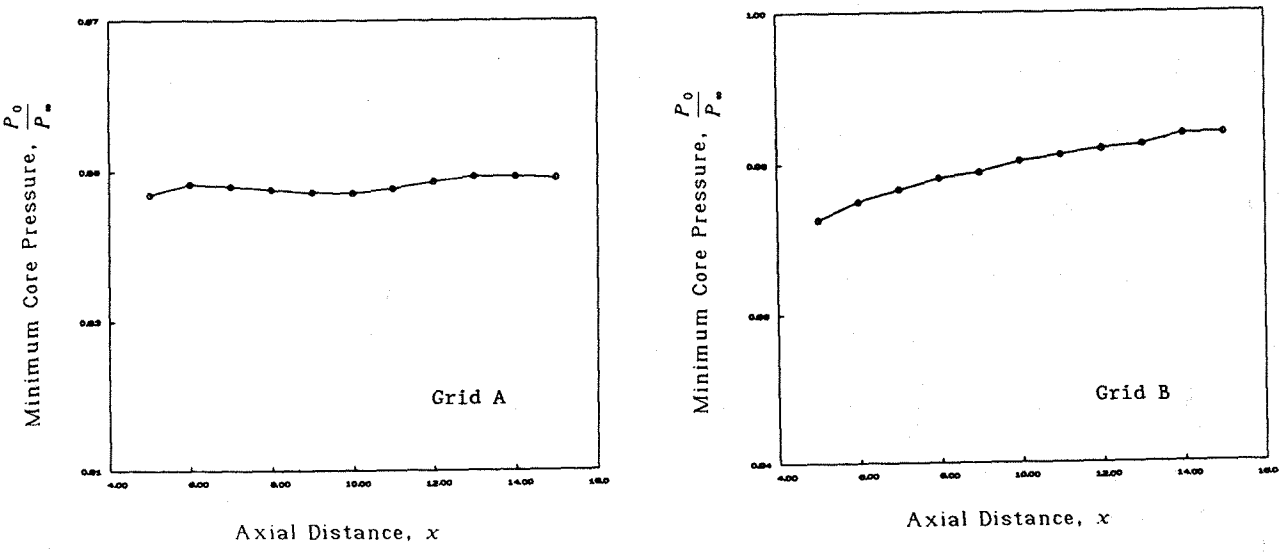

Figure 5. Comparison of axial pressure distributions for Euler solutions with identical initial and boundary conditions but different grids.

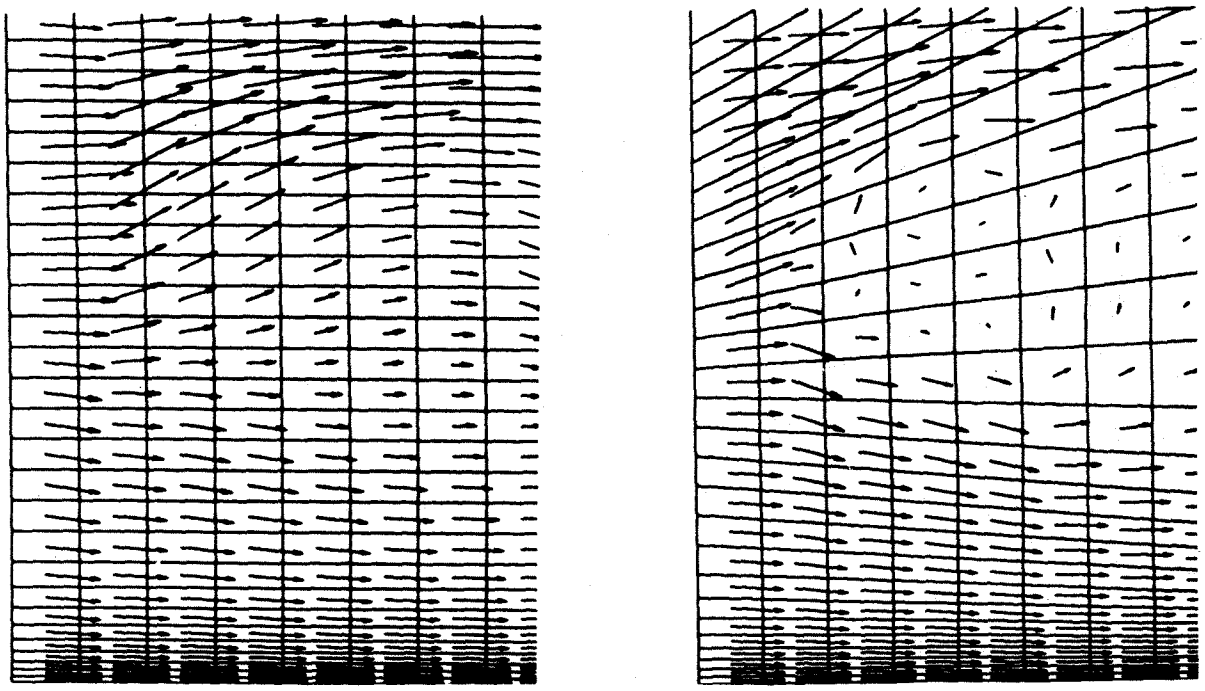

Figure 6. Side views of velocity vectors in the vertical plane containing the vortex axis for identical flow conditions on the two grids of figure 4.

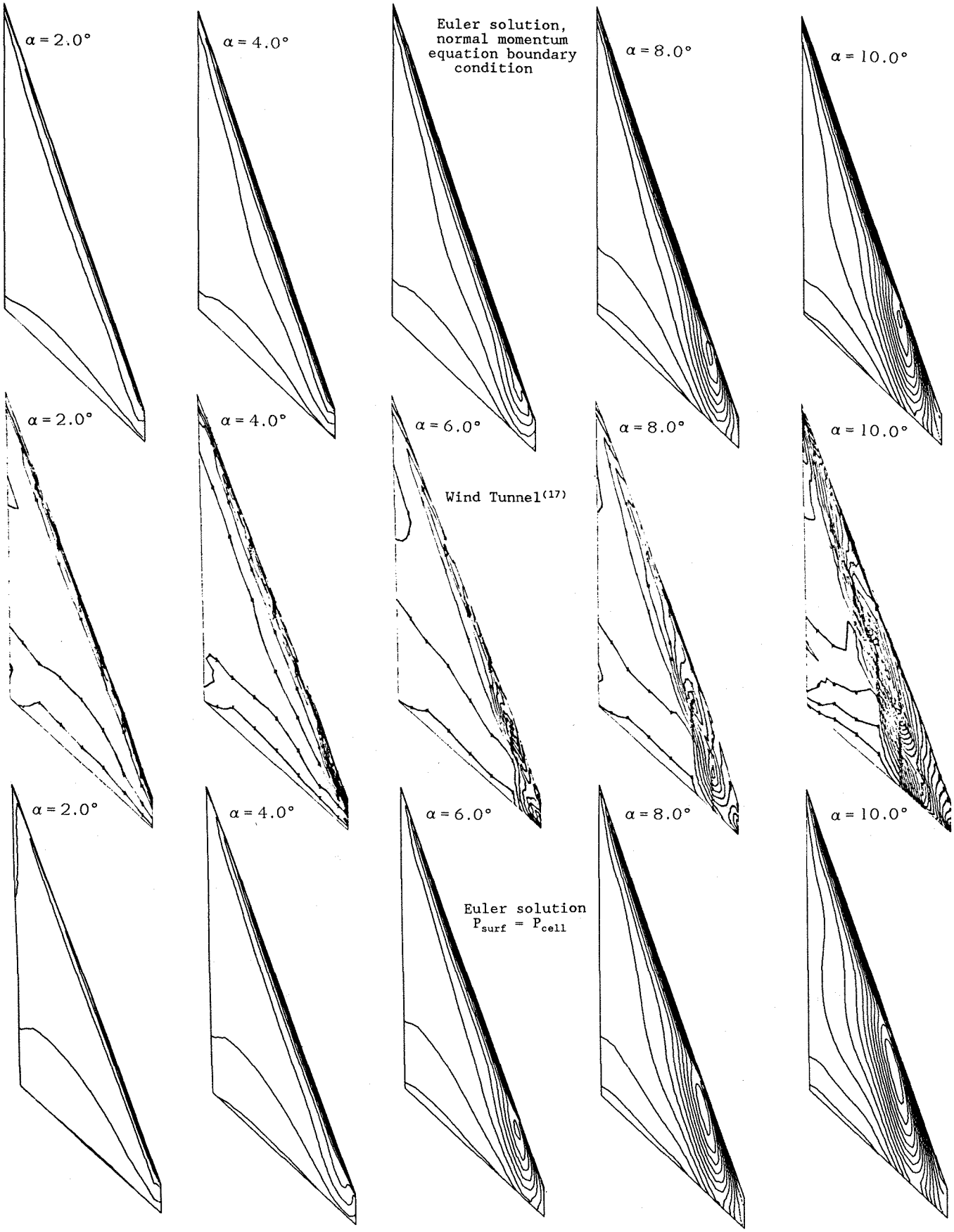

Figure 7. Comparison of surface pressure contours on an arrow wing for wind tunnel tests[16] and two Euler solutions with different surface boundary conditions.

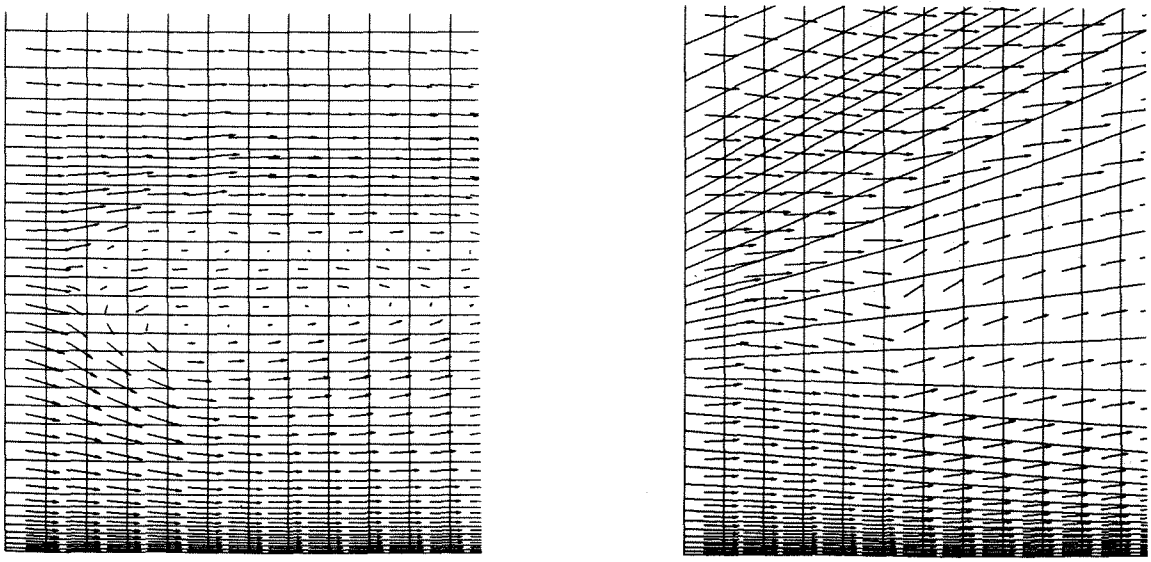

Grid A

Grid B

Figure 8. Side views of velocity vectors in the vertical plane containing the vortex axis for flow solutions on grids A and B. The vortex core model has been used to cause vortex bursting on grid A and prevent bursting on grid B.

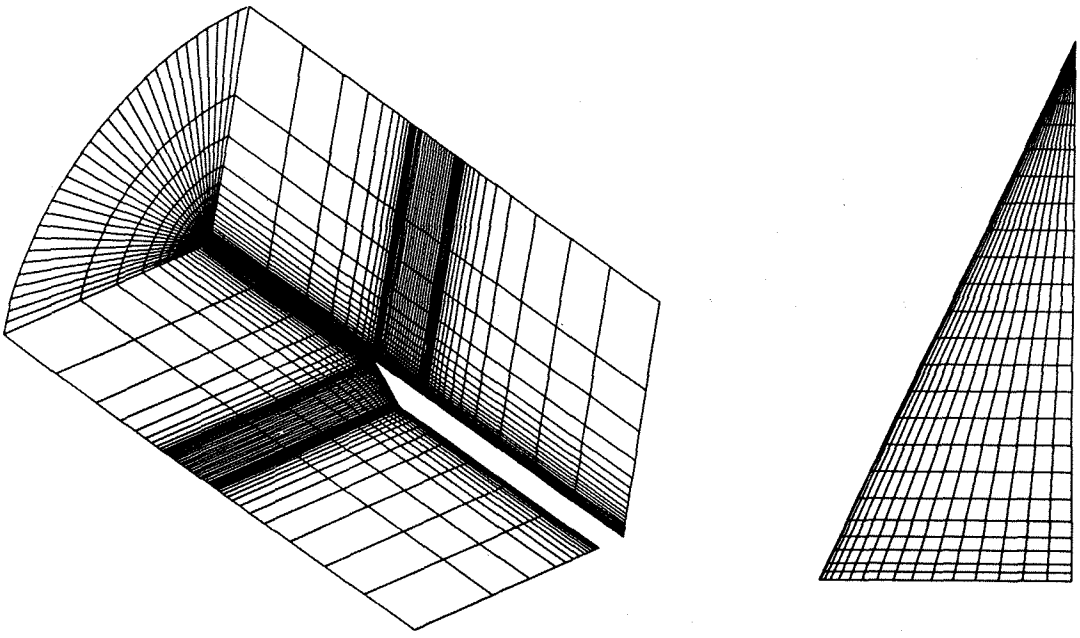

Figure 9. Typical H-O grids used for the vortex bursting study.

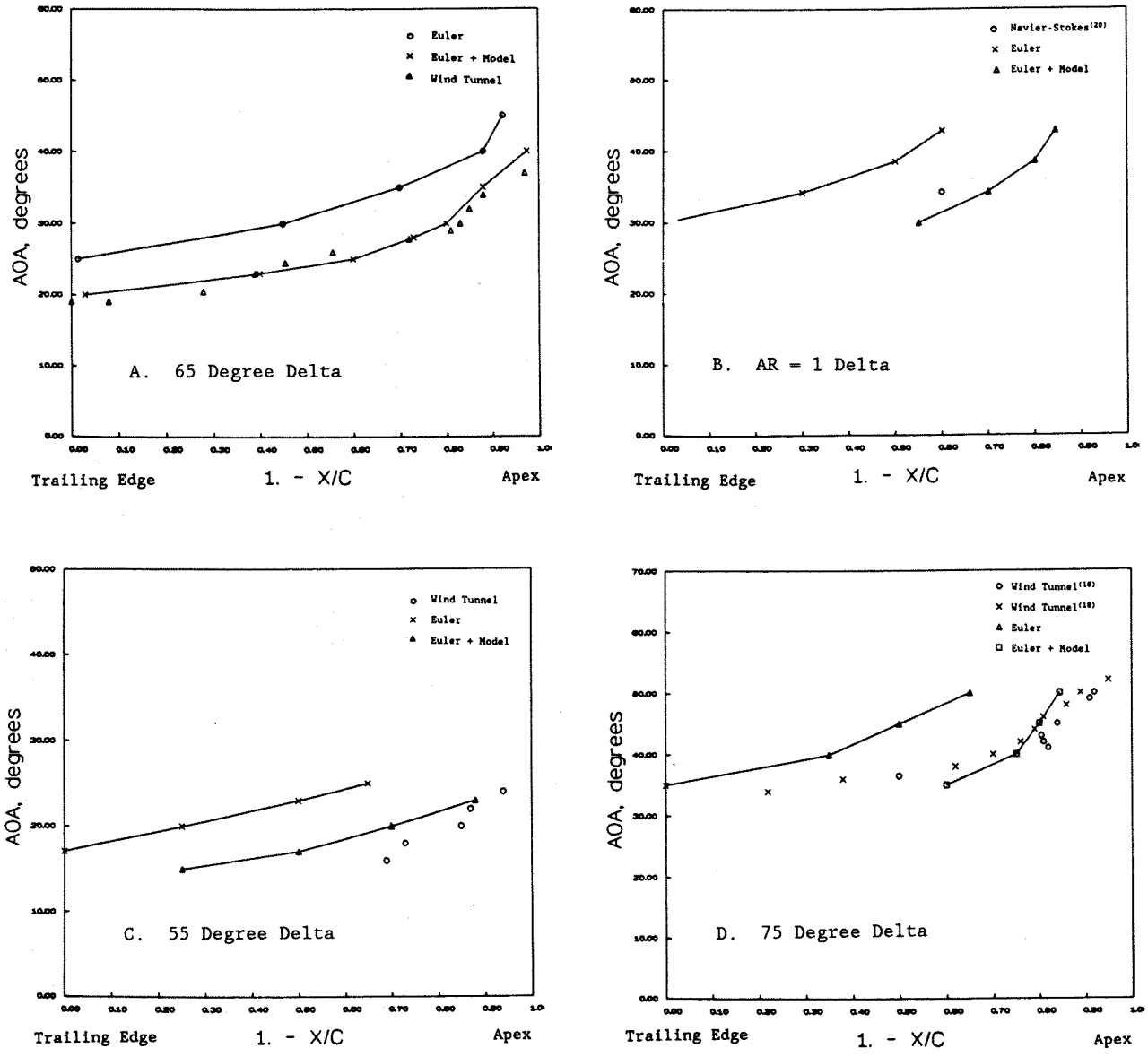

Figure 10. Bursting location vs angle of attack curves for four different delta wings obtained from wind tunnel experiments,[18,19] Navier-Stokes solutions[20] and Euler solutions with and without the vortex core model.

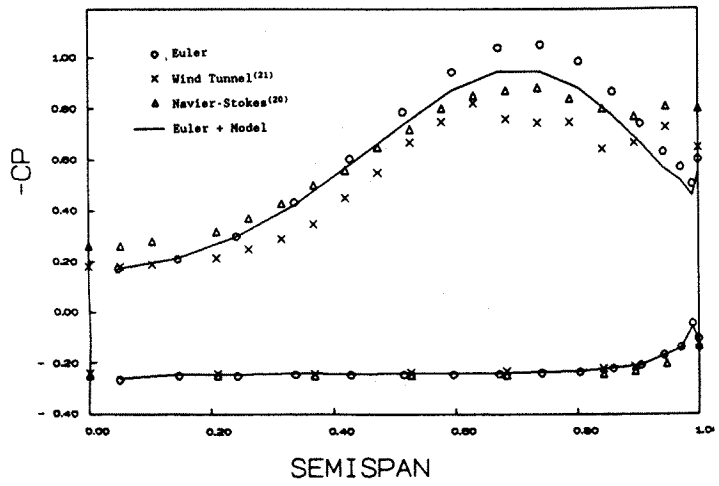

Figure 11. Comparison of pressure coefficient curves at X/C = 0.7 obtained from four methods for an AR = 1 delta wing at 20.5 degrees angle of attack.

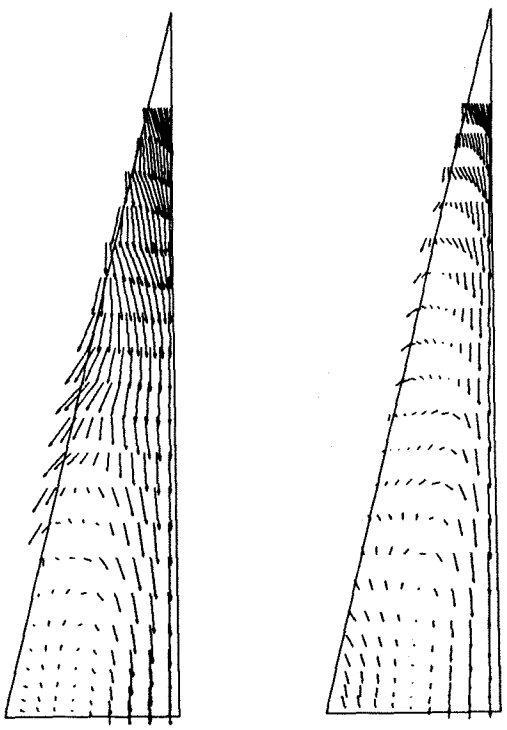

Euler

Euler + Model

Figure 12. Planform views of velocity vectors in the horizontal plane of the leading edge vortex over an AR = 1 delta wind at 40 degrees angle of attack.

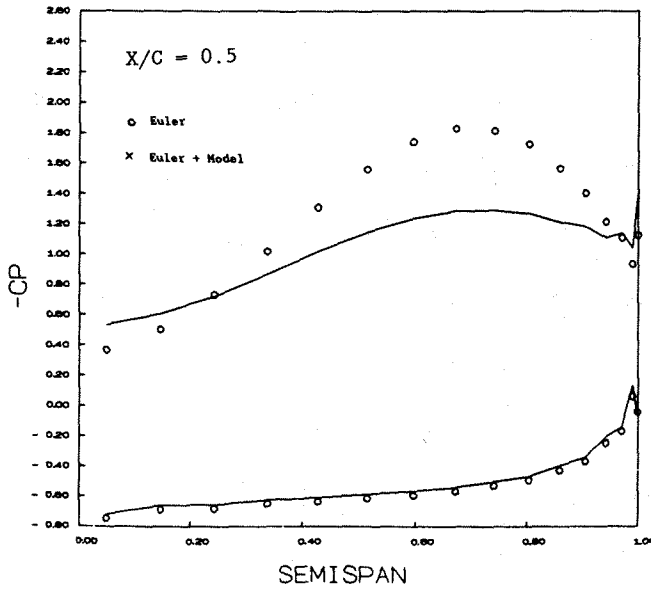

Figure 13. Comparison of pressure coefficient curves at X/C = 0.5 for the two cases of figure 12.

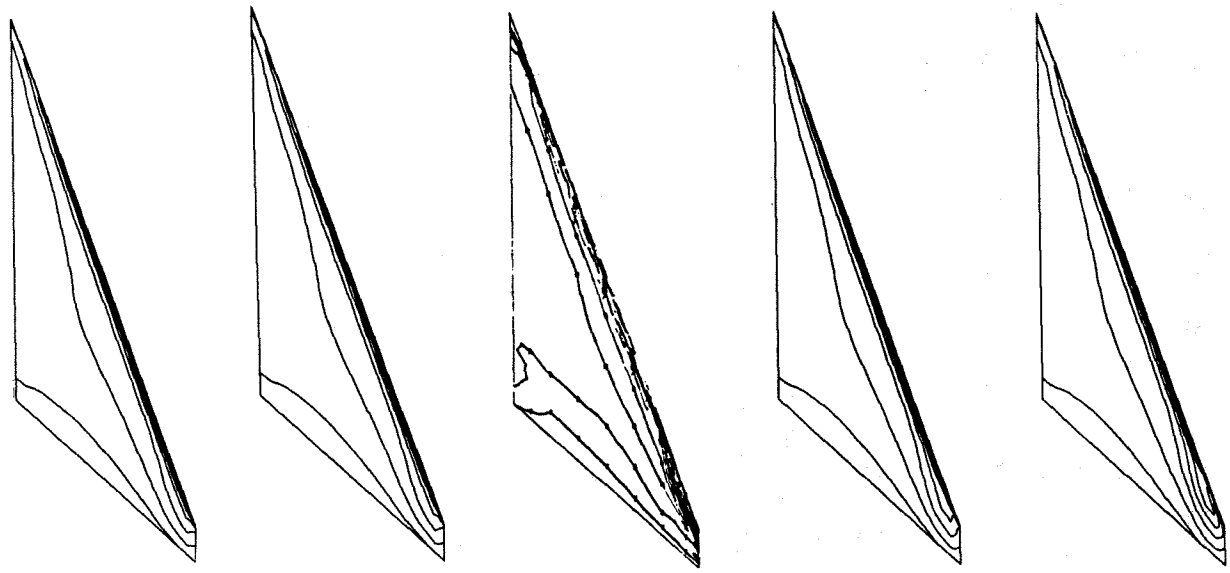

$K_\delta = 1.3$ $K_\delta = 2.1$ Wind Tunnel[17] $K_\delta = 3.3$ $K_\delta = 5.3$

Figure 14. Wing surface pressure contours for a range of values of the viscous layer growth parameter compared with wind tunnel data. Angle of attack is 4 degrees.

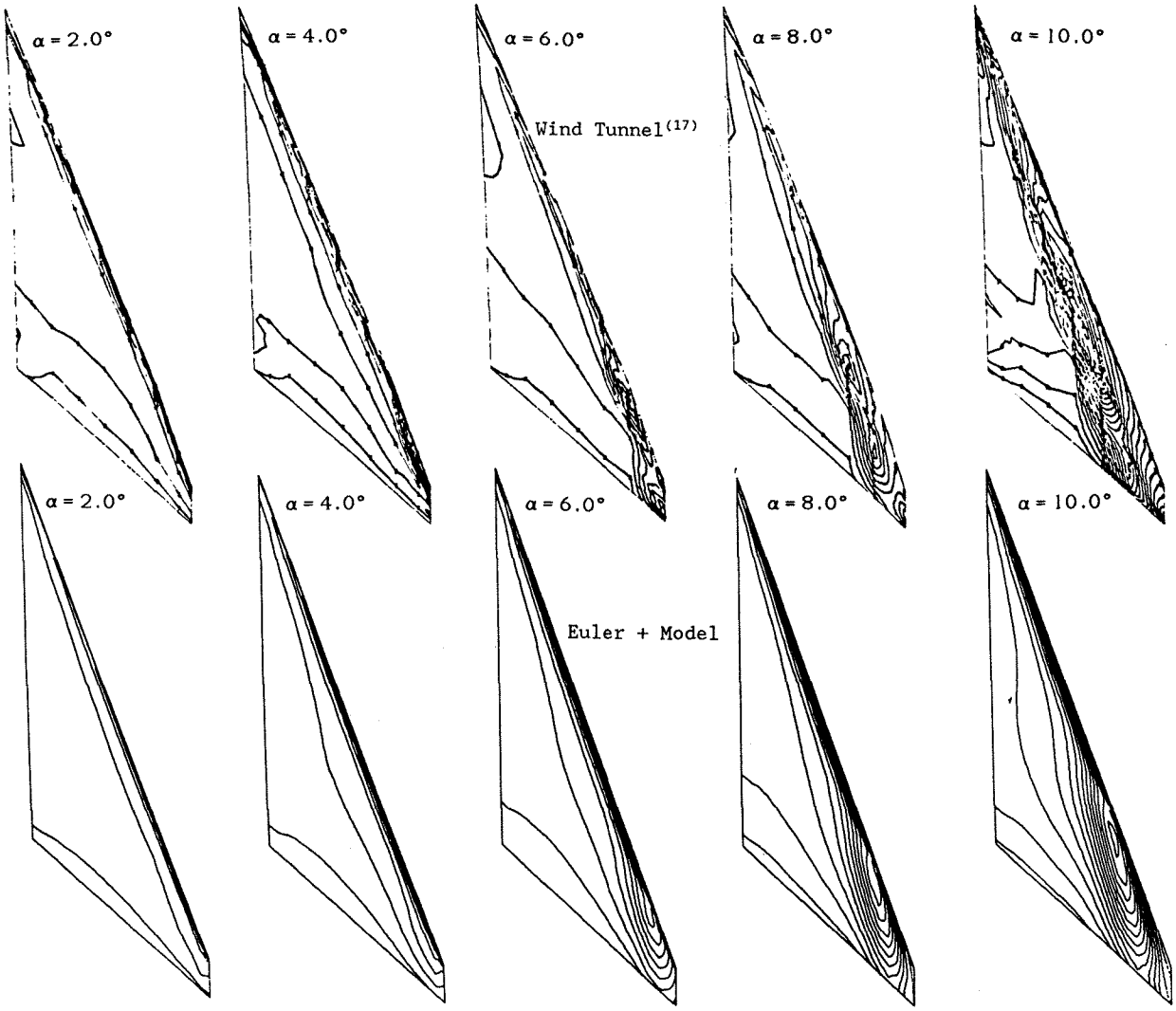

Figure 15. Comparison of wing surface pressure contours for wind tunnel tests and results from the Euler solver with modified surface boundary condition.

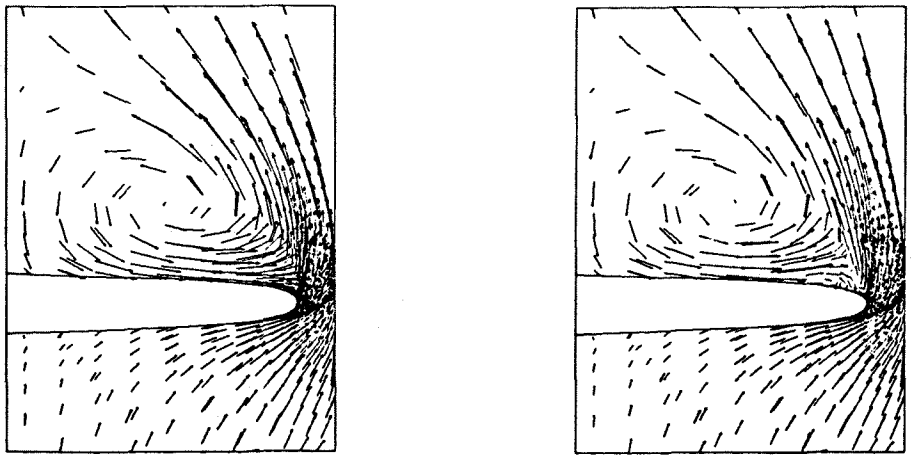

(A) Euler

(B) Euler + Model

Figure 16. Crossflow plane velocity vectors at X/C = 0.5 on 65 degree round leading edge delta for Euler alone and Euler with velocity defect model.